

# Interfibrillar packing of bovine cornea by table-top and synchrotron scanning SAXS microscopy

T. Sibillano,<sup>a</sup> L. De Caro,<sup>a</sup> F. Scattarella,<sup>b</sup> G. Scarcelli,<sup>c</sup> D. Siliqi,<sup>a</sup> D. Altamura,<sup>a</sup> M. Liebi,<sup>d</sup> M. Ladisa,<sup>a</sup> O. Bunk<sup>c</sup> and C. Giannini<sup>a\*</sup>

<sup>a</sup>Istituto di Cristallografia (IC-CNR), via Amendola 122/O, Bari, I-70126, Italy, <sup>b</sup>IOM CNR Laboratorio TASC, Area Science Park – Basovizza, Bld MM SS 14, Trieste, 34149, Italy, <sup>c</sup>Fischell Department of Bioengineering, University of Maryland, College Park, MD 20742, USA, and <sup>d</sup>Paul Scherrer Institut, Swiss Light Source, 5232, Villigen PSI, Switzerland.

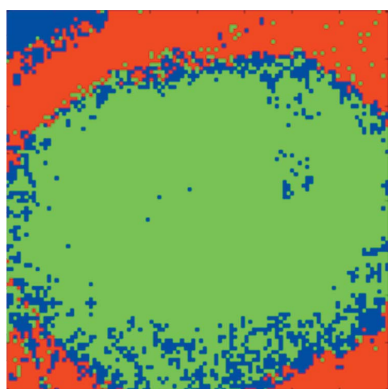
\*Correspondence e-mail: cinzia.giannini@ic.cnr.it

Bovine cornea was studied with scanning small-angle X-ray scattering (SAXS) microscopy, by using both synchrotron radiation and a microfocus laboratory source. A combination of statistical (adaptive binning and canonical correlation analysis) and crystallographic (pair distribution function analysis) approaches allowed inspection of the collagen lateral packing of the supramolecular structure. Results reveal (i) a decrease of the interfibrillar distance and of the shell thickness around the fibrils from the periphery to the center of the cornea, (ii) a uniform fibril diameter across the explored area, and (iii) a distorted quasi-hexagonal arrangement of the collagen fibrils. The results are in agreement with existing literature. The overlap between laboratory and synchrotron-radiation data opens new perspectives for further studies on collagen-based/engineered tissues by the SAXS microscopy technique at laboratory-scale facilities.

## 1. Introduction

Cornea is a connective transparent tissue comprising about 70% collagen, the majority of which is in the form of a layered network of ordered fibrils embedded in a proteoglycan-rich extrafibrillar matrix (Meek & Quantock, 2001). The collagen fibrils are mainly contained in the stroma, the thickest layer of the cornea. Immunocytochemical studies (Marshall *et al.*, 1991*a,b*) showed the existence of several types of collagen in cornea, both in fibril- (type I, III and V) and in non-fibril-forming molecules (type VI and XII) (Zimmermann *et al.*, 1986; Zhan *et al.*, 1990). The hybrid nature of the collagen fibrils, especially for the presence of type V molecules, has a high influence on the fibril diameters (Birk *et al.*, 1990).

The main geometrical properties of the cornea, that is its shape and curvature, as well as its microscopic and nanoscopic structure, have been widely investigated using several characterization techniques, like optical and electron microscopy, and clinical confocal microscopy (Komai & Ushiki, 1991; Dhaliwal & Kaufman, 2009; Meek & Fullwood, 2001). The mechanical strength of the cornea together with its refractive index and transparency are directly related to the collagen arrangement in its lamellar structure, each lamella containing long collagen fibrils of uniform diameter (Scarcelli *et al.*, 2012). At the ultrastructural level, the cornea has been studied over the past 60 years mostly by electron microscopy and X-ray diffraction to investigate the fine structure of the collagenous lamellae comprising the stroma. However, many divergences were observed between the results arising from electron microscopy and other characterization techniques, mainly due to the different conditions of preparation and measurement of



the samples (Dhaliwal & Kaufman, 2009). Nowadays, the development of new microscopies, such as second-harmonic generation multi-photon imaging (Aptel *et al.*, 2010; Masters, 2009) as well as X-ray microscopy, has allowed the quantitative investigation of the organization of the fibril-forming collagen in cornea. In particular, both small- and wide-angle X-ray scattering (SAXS and WAXS) allow the collection of structural quantitative data from the entire cornea and across its full thickness. The SAXS signal from axially aligned fibrils in each lamella can provide a quantitative evaluation of the diameter ( $\varphi$ ) and the lateral interfibrillar spacing ( $L$ ), along the equatorial direction, and of the  $D$  periodicity along the fibril axis, which coincides with the meridional direction (Boote *et al.*, 2013; Meek & Fullwood, 2001). The presence of the equatorial contribution in SAXS patterns of cornea is due to the uniform diameter of the collagen fibrils in cornea and to a short-range order in their lateral arrangement.

The WAXS signal, produced by the intrafibrillar structure of the collagen, allows the evaluation of the orientation and distribution of the collagen molecules and the intermolecular spacing (Boote *et al.*, 2011, 2013).

The fibril packing was initially ascribed to a regular (hexagonal) lattice in which lamellae, acting as diffraction gratings for the incident radiation, are composed of collagen fibrils of uniform diameter (Maurice, 1957, 1962, 1984).

However, later studies based on electron microscopy and X-ray diffraction have suggested that the fibrils are not arranged in a perfect lattice but rather in a liquid-like paracrystalline system marked out by a short-range order, essential for corneal transparency. Several mathematical formulations of corneal transparency have thus tried to prove that the paracrystalline structure derived from electron micrographs and X-ray diffraction can give rise to transparency (Birk *et al.*, 1990; Boote *et al.*, 2003; Meek & Fullwood, 2001).

The organization of the proteoglycan-based extrafibrillar matrix is fundamental for the regular arrangement of the collagen fibrils in the stroma (Quantock *et al.*, 1990). The model developed by Maurice (1962) outlined a structure in which each collagen fibril is connected with six neighboring fibrils by means of proteoglycans, leaving a regular spacing between fibrils. A refined version of this model (Maurice *et al.*, 2004) showed that the six proteoglycans are attached orthogonally to the fibrils, each of them characterized by a  $\varphi$  diameter of around 23 nm, and connect the collagen fibrils to each other. The combined arrangement of proteoglycans and fibrils forms a ring-like structure of core-shell cylinders with a shell thickness of  $\sim 11$  nm and an interfibrillar spacing  $L$  of  $\sim 45$  nm. More recently, Cheng & Pinsky (2013) developed a theoretical analysis of the forces exerted by the proteoglycans to maintain the short-range order of the collagen fibrils in the cornea.

All these models provide a good explanation of the stromal transparency, the observed high structural birefringence and the clouding of the cornea tissue under stress, together with the uniformity of the collagen fibril packing (Meek *et al.*, 1991). More recently (Lewis *et al.*, 2010; Meek & Knupp, 2015) a model has been developed based on the three-dimensional

tomographic reconstructions of bovine cornea, showing the collagen fibrils not lying according to a perfect hexagonal lattice. Indeed, the distribution of distances between adjacent fibrils was narrow and these distances were the result of two opposing forces acting on the fibrils by the proteoglycans. Therefore, the whole cornea has a less rigid and more fluid overall structure, with the collagen fibrils arranged as in a Fibonacci quasi-crystal (Meek & Knupp, 2015).

Also, the distribution of water in the fibrils and in the lamellae can influence the mechanical properties of the cornea (Fratzl & Daxer, 1993). An X-ray study on the swelling process of the human cornea has been conducted by Meek *et al.* (1991) by measuring the intermolecular and interfibrillar spacings of collagen in the bovine cornea from wide- and small-angle X-ray diffraction patterns as a function of tissue hydration. The interfibrillar spacing increased from  $L \simeq 34$  nm in completely dried corneas to  $L \simeq 64$  nm at normal hydration, and the intermolecular spacing increased from  $d \simeq 1.15$  nm to  $d \simeq 1.60$  nm, respectively. Both distances continued to increase slowly for hydration above the normal condition, suggesting that the interfibrillar spacing and the intermolecular packing are correlated and shift simultaneously with hydration. In greater detail, at the beginning of the hydration process the water flows within and between the fibrils, whereas above normal hydration water does not fill the interfibrillar space uniformly but goes preferentially between the fibrils rather than within them. X-ray scattering studies on the correlation between degree of hydration and the characteristics of the human cornea were also conducted by Fratzl & Daxer (1993) by drying rather than swelling the tissue.

The anisotropy of the fibrillary structure in terms of both fibril spacing and diameter as a function of the position across the cornea has also been evaluated in several papers, especially for the human cornea (Boote *et al.*, 2003, 2011; Meek *et al.*, 2005). The studies demonstrated that the fibril packing is not uniform over the corneal surface and is more compact in the prepupillary cornea compared with peripheral and limbus zones, showing a smaller center-to-center fibril spacing but a constant diameter of the fibrils. The higher packing density of collagen fibrils in the center of the cornea was directly correlated to the higher refractive index of the stroma, responsible for the maintenance of the tissue strength and curvature in this thinner zone. X-ray scattering has also been used to investigate the alteration of the ultrastructure of the cornea in the presence of selected diseases and disorders. A number of papers focused on the study of the diameter and the intermolecular and interfibrillar spacing in the presence of bullous keratopathy or Fuchs' dystrophy with edema (Quantock *et al.*, 1991), several types of mucopolysaccharidose disorders (Quantock, Meek, Fullwood *et al.*, 1993; Huang *et al.*, 1996; Rawe *et al.*, 1997), and macular corneal dystrophy and granular corneal dystrophy (Meek *et al.*, 1989; Quantock, Meek, Thonar *et al.*, 1993; Quantock *et al.*, 1997). Among these studies, the understanding of the collagen alterations in keratoconus is of particular interest.

Keratoconus causes progressive thinning of the stroma and consequently abnormal curvature, inducing irregular astig-

matism and myopia, corneal fibrosis, and distortion of vision, due to the modification in the organization of the corneal collagen. Daxer & Fratzl (1997) first demonstrated how the symptoms of this disease were strictly correlated with an alteration of the preferred collagen orientations at the center of the cone. Maps of the orientation of the stromal lamellae and the relative distribution of collagen fibrillar mass in keratoconus were compared with those of normal corneas, and showed a high degree of inter- and intralamellar displacement and slipping. These findings explained well the pathologic area in the cornea caused by a loss of cohesion between collagen fibrils along the axis of the lamellae and the non-collagenous matrix (Meek *et al.*, 2005). *Ex vivo* and *in vivo* studies on human healthy and keratoconic corneas by means of Brillouin measurements have recently demonstrated that a reduced mechanical stability is concentrated within the area of the keratoconic cone (Scarcelli *et al.*, 2014, 2015).

Cross-linking of collagen refers to the ability of collagen fibrils to form stronger chemical bonds with adjacent fibrils. This effect naturally occurs in the cornea with age and causes the enhancement of its strength and stiffness. A new technique for artificial collagen cross-linking (CXL) (Spoerl *et al.*, 1998; Wollensak *et al.*, 2003*a,b*) is based on the photopolymerization of stromal collagen fibers induced by the combined action of the riboflavin, a photosensitizing substance, and the ultraviolet UVA radiation incident on the de-epithelialized surface of the cornea. This causes a significant increase in corneal stiffness, as demonstrated in studies on animals using stress-strain mechanical measurements (Wollensak *et al.*, 2003*a,b*), assessing the resistance against enzymatic digestion (Spoerl *et al.*, 2004) or measuring the longitudinal elastic modulus (Scarcelli *et al.*, 2014). Several studies showed that the CXL treatment is efficient in stopping the progression of keratoconus disease, and the increased stiffness of the cornea is widely believed to be a major determinant of the treatment's effectiveness (Wollensak, 2006; Snibson, 2010). However, the mechanism by which UV-CXL increases the stiffness of the cornea is not completely understood and is probably due to an increase in the number of intrafibrillar and interfibrillar covalent bonds in corneal collagen.

Studies based on SAXS measurements, hydrodynamic behavior and enzymatic digestion showed no correlation between the riboflavin/UVA-CXL treatment and the change of the intermolecular spacing, the collagen fibril diameter and the *D* period of corneal collagen (Hayes *et al.*, 2011), different to what was reported in a previous study (Meek *et al.*, 2008).

This evidence supports the idea that the therapy does not promote a cross-linking of molecules throughout the fibrils, but it does not exclude the possibility of cross-linking within and/or between collagen molecules at the surface of fibrils, which accords with the observed enhancement of the bio-mechanical properties and resistance of enzymatic digestion after treatment.

A key issue in most of the cited X-ray diffraction experiments is the need for high-brilliance synchrotron-radiation X-ray sources, to obtain high-quality scattering patterns and therefore to yield qualitative and quantitative information on

the collagen fibrils across the width of the cornea and through its depth, over several mm<sup>2</sup>. X-ray methods have the essential advantage, over electron and other microscopies, that samples can be investigated close to physiologic hydration. Therefore, no prior treatment such as dehydration or embedding is required. Indeed, several papers have shown how the preparative procedures induce changes in the corneal ultra-structure (Fullwood & Meek, 1993).

Today, thanks to the recent developments of table-top X-ray microsources, new opportunities are available to obtain quantitative information about the arrangement of the lamellae and fibrils with a spatial resolution of a few tens of micrometres, also in room-sized laboratories. In our previous papers (De Caro *et al.*, 2012, 2013; Sibillano *et al.*, 2014) we demonstrated the effective combination of a table-top superbright microfocus X-ray source and a restoration algorithm for the investigation of soft natural engineered tissues as well as inorganic nanomaterials, by means of SAXS/WAXS experiments realized in a room-sized laboratory. Interesting performance and flexibility have been demonstrated in *ex situ* grazing-incidence SAXS (Altamura, Holý *et al.*, 2012) on self-assembled nanoscale inorganic superstructures, as well as in *ex situ* SAXS experiments on air-dried rat tail tendon (De Caro *et al.*, 2012), and residues of cell exosomes and artificial collagen scaffolds (Sibillano *et al.*, 2014).

Here, we investigate a bovine cornea by SAXS scanning microscopy, with the aim of setting up a procedure able to derive the collagen supramolecular structure. The proposed methodology, based on the combination of statistical and crystallographic approaches, demonstrates the possibility of performing structural change studies of corneal tissues in room-sized laboratories, after chemical/physical treatments. The correctness of the adopted methodology is deduced by comparing synchrotron-radiation data with table-top X-ray microsource data, besides the abundant data from the literature.

## 2. Experimental

### 2.1. Sample preparation

A bovine whole eye (~1 year old) was obtained 2–4 h post-mortem (Research 87 Inc., Boylston, MA, USA) and preserved at 277 K until the beginning of the UV-CXL procedure. For the cross-linking procedure, the corneal epithelium in the central portion (diameter ~10 mm) of the bovine eye was removed by gentle scraping with a blade (Parker 15; BD Biosciences, San Diego, CA, USA). The cross-linking agent riboflavin (riboflavin-5-phosphate; Sigma-Aldrich, St Louis, MO, USA) was diluted in phosphate-buffered saline to a riboflavin solution of 0.1%, in order to keep the corneal thickness constant during the CXL procedure. The cornea without epithelium was fully soaked in the riboflavin solution for 10 min. Excess riboflavin on the tissue surface was washed away with saline solution. Corneas were then exposed to UV irradiation (wavelength 365 nm, 3 mW cm<sup>-2</sup>) for 30 min. During irradiation, a drop of ribo-

flavin solution was applied to the cornea every 5 min. After corneal cross-linking, the tissue was again washed out with saline solution and dried with a paper cloth. Finally, the corneas were surgically extracted from the eye-ball and fixed in 10% formalin, following the standard procedure used for histologic analysis. The corneas were then shipped within the same formalin solution for the X-ray investigations.

### 2.2. Synchrotron-radiation experiments

Scanning SAXS experiments were performed at the cSAXS beamline (Bunk *et al.*, 2009) of the Swiss Light Source (SLS), Paul Scherrer Institut, Villigen, Switzerland. A monochromatic X-ray beam ( $\lambda = 0.09116$  nm,  $E = 13.6$  keV) was focused down to about  $30 \times 15$   $\mu\text{m}$  by a bent monochromator crystal and a bent mirror. The corneas, kept in formalin within a Kapton sachet, were placed perpendicular to the direct beam and raster scanned through the beam spot, with the detector measuring the total intensity coming from the currently illuminated spot on the sample, integrated over the exposure time and across the sample thickness. Step sizes of 100  $\mu\text{m}$  in both the horizontal and the vertical directions, and exposure times of 0.1 s, were used. To speed up acquisition, data were recorded in a continuous line-scan mode where the sample is moved at constant speed along a line of the two-dimensional raster scan, with the Pilatus 2M detector (Bunk *et al.*, 2009) continuously recording data. SAXS data were collected at a sample–detector distance of 7126 mm.

### 2.3. Laboratory experiments

Scanning SAXS experiments were also performed at the XMI-L@b of the Institute of Crystallography, National Research Council, Bari, Italy. The XMI-L@b has a Rigaku three pinhole camera (SMAX-3000) coupled to a Fr-E+ SuperBright rotating copper anode microsource (2475 W, copper radiation Cu  $K\alpha$ ,  $\lambda = 0.15405$  nm, 8 keV) by means of multilayer focusing optics (Confocal Max-Flux; CMF 15–105). The X-ray beam can be focused down to about  $70 \times 70$   $\mu\text{m}$  (small spot configuration) or down to  $200 \times 200$   $\mu\text{m}$  (large spot configuration). The cornea, kept in formalin within a Kapton sachet, was placed perpendicular to the direct beam and raster scanned vertically and horizontally through the beam spot, with the detector measuring the total intensity coming from the currently illuminated spot on the sample. The diffraction signal is integrated over the exposure time and across the sample thickness. Step sizes of 100  $\mu\text{m}$  (small spot) and 300  $\mu\text{m}$  (large spot) in both the horizontal and the vertical directions, and exposure times of 150 s, were used. The detection system was a Triton 20 gas-filled proportional counter ( $1024 \times 1024$  array, 195 mm pixel size). SAXS data were collected at a sample–detector distance of 2200 mm (Altamura, Lassandro *et al.*, 2012). Table 1 summarizes the most important experimental details of the table-top (XMI-L@b) and synchrotron (cSAXS) experiments.

**Table 1**

Relevant experimental details used for table-top (XMI-L@b) and synchrotron (cSAXS) experiments.

	XMI-L@b (IC-CNR)	cSAXS (SLS)
Energy (keV)	8	13.6
Wavelength ( $\text{\AA}$ )	1.54	0.91
Flux (photon $\text{s}^{-1}$ )	$\sim 10^7$	$\sim 10^{12}$
Beam size ( $\mu\text{m}$ )	$70 \times 70$	$30 \times 15$
Pixel size ( $\mu\text{m}$ )	195	172
Sample–detector distance (mm)	2200	7126
Beam stopper size (mm)	5.5	3
$q_{\text{min}}$ ( $\text{\AA}^{-1}$ )	0.005	0.0017
$d_{\text{max}} = 2\pi/q_{\text{min}}$ (nm)	125	370
Exposure time per point (s)	150	0.1

## 3. Results

The bovine cornea that underwent the UV-CXL procedure was studied by SAXS scanning microscopy at both laboratories described in §2. Comparable areas, namely  $10 \times 10$  mm at cSAXS and  $8 \times 10$  mm at XMI-L@b, were explored.

The analysis of SAXS scanning microscopies was performed by the *SUNBIM* software (Siliqi *et al.*, 2016). Each of the two-dimensional SAXS frames was calibrated by a silver behenate sample (Blanton *et al.*, 1995), azimuthally integrated and folded into a one-dimensional intensity profile. Two sets of data were collected, referred to from now on as the cSAXS-SLS and XMI-L@b data sets, respectively. The adaptive binning (ADB) method (Guagliardi *et al.*, 2007) was then applied to look for a finite number of representative profiles in the entire set of measurements. Fig. 1(a) shows the profiles (from now on called the cSAXS-SLS reference data) selected by ADB from the cSAXS-SLS data set. Here, the blue line is the contribution coming from the region outside the corneal tissue, whereas the red and the green profiles correspond to typical collagen fiber diffraction spectra for the regions with and without epithelium, respectively. The sharpest peaks in both red and green curves correspond to the expected meridional reflections of the type I collagen scattering profile, due to the 65 nm periodicity along the fibril axis (marked with dotted vertical lines). The broader peaks identify the equatorial reflections that carry information about the fibril diameters and the interfibrillar distances (lateral collagen packing). The red and green profiles shown in Fig. 1(a), corresponding to cSAXS-SLS reference data 1 and cSAXS-SLS reference data 2, respectively, are identical in terms of the meridional diffraction peak position and differ only in the equatorial scattering. The insets in Fig. 1(a) show the two-dimensional SAXS frames corresponding to each representative profile.

A canonical correlation analysis (CCA) (Hotelling, 1936) was performed across (thousands of) azimuthally integrated one-dimensional profiles of the cSAXS-SLS data set. CCA is a multichannel generalization of ordinary correlation analysis, which quantifies the relationship between two random variables  $x$  and  $y$  by means of the so-called correlation coefficient, a scalar quantity with a value between  $-1$  and  $1$  that measures the degree of linear dependence between  $x$  and  $y$ .

When applying correlation analysis to SAXS data, the variables  $x$  and  $y$  need to be specified. In ordinary correlation analysis,  $x$  and  $y$  are univariate variables and, in our case, the  $x$  variable consists of each one-dimensional profile of the entire cSAXS-SLS data set, whereas the  $y$  variable is one of the three representative cSAXS-SLS reference profiles in Fig. 1(a). The result of this statistical screening is plotted in Fig. 1(b), where the red corona and the green central part display the actual distribution of the cSAXS-SLS reference data across the explored area. The ADB analysis was also done on the laboratory data set, and three representative profiles were consequently extracted (henceforth referred to as the XMI-L@b reference data) and compared in Figs. 1(c) and 1(d) with the corresponding cSAXS-SLS reference data. The lower X-ray source coherence and intensity are reflected in a lower visibility of the meridional peaks in the XMI-L@b reference data. A similar procedure was also applied to the XMI-L@b data set; the resulting segmentation map showed a red color in the outer corona without the epithelium layer and a green one in the center of the cornea (data not shown).

The main difference between the green and red profiles in Fig. 1(a) is due to the equatorial scattering, as can be clearly recognized in Fig. 1(a), where meridional peaks (marked by the vertical lines) keep the same position in both the green

and the red patterns, whereas the equatorial peaks shift to lower  $q$  values in the red pattern. Therefore, we applied a selective filter to the cSAXS-SLS reference data in order to remove the meridional contribution from the 65 nm periodicity. Technically, one can extract the equatorial signal from the whole diffraction pattern by considering it as the background of the whole spectrum. When the meridional diffraction peaks are very weak it is not necessary to eliminate them from the experimental data. Therefore, this filtering procedure was applied only on the SLS experimental data. The result of this filtering is shown in Figs. 1(c) and 1(d) (left panels, black lines) for the cSAXS-SLS reference data. A de-noising procedure (Siliqi *et al.*, 2016) was applied to the XMI-L@b reference data, after the two-dimensional raw data were azimuthally integrated into one-dimensional profiles. The de-noised patterns are shown as black lines in Figs. 1(c) and 1(d) (right panels). For each profile of the cSAXS-SLS and XMI-L@b reference data, the background was linearly interpolated and used for the following analysis.

Fig. 2(a) shows the cSAXS-SLS filtered data [same black curves in Figs. 1(c) and 1(d)]. In order to interpret the data, we calculated the pair distribution function (PDF) of the red and green profiles by the *PDFGETX3* program (Juhás *et al.*, 2013). The software computes the Fourier transform of the diffracted

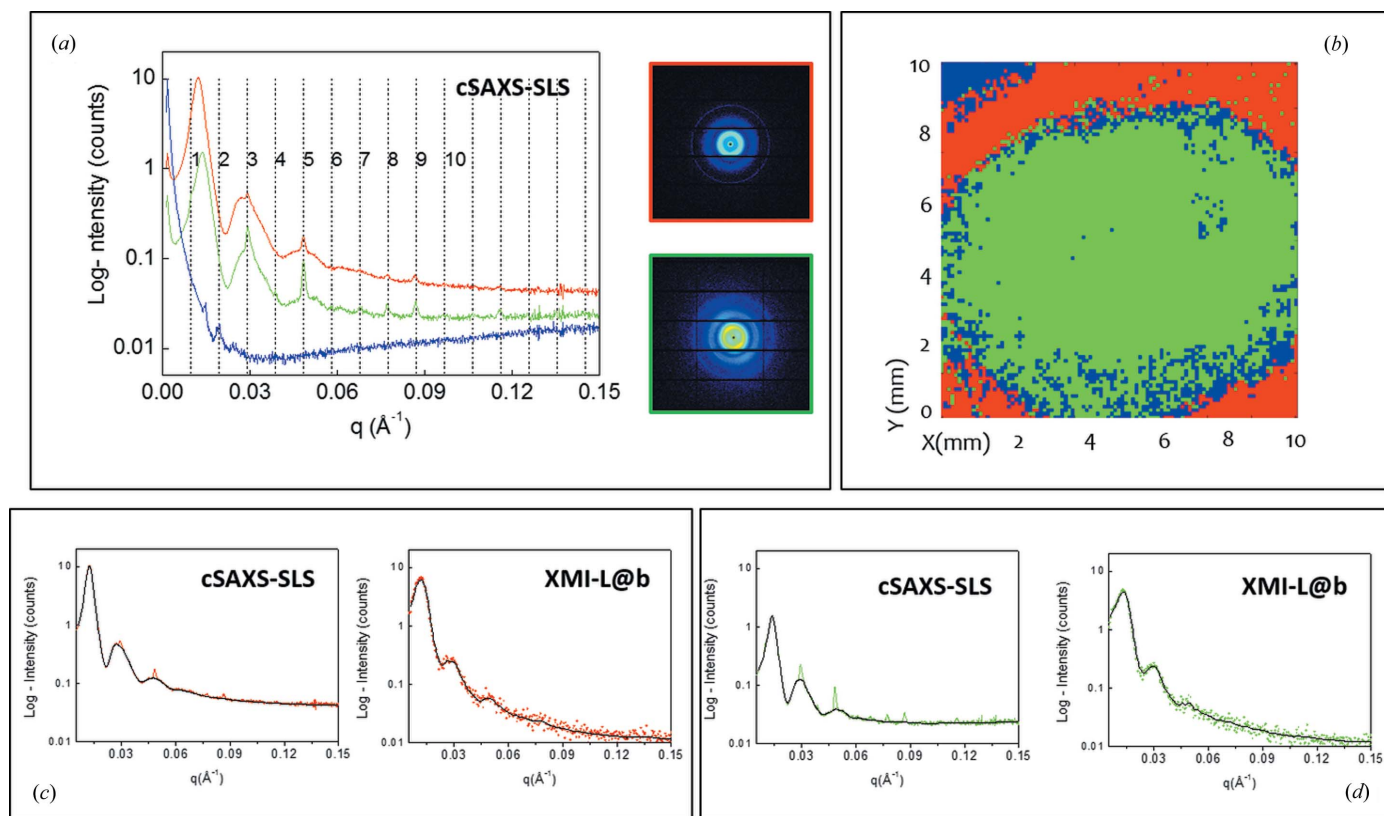
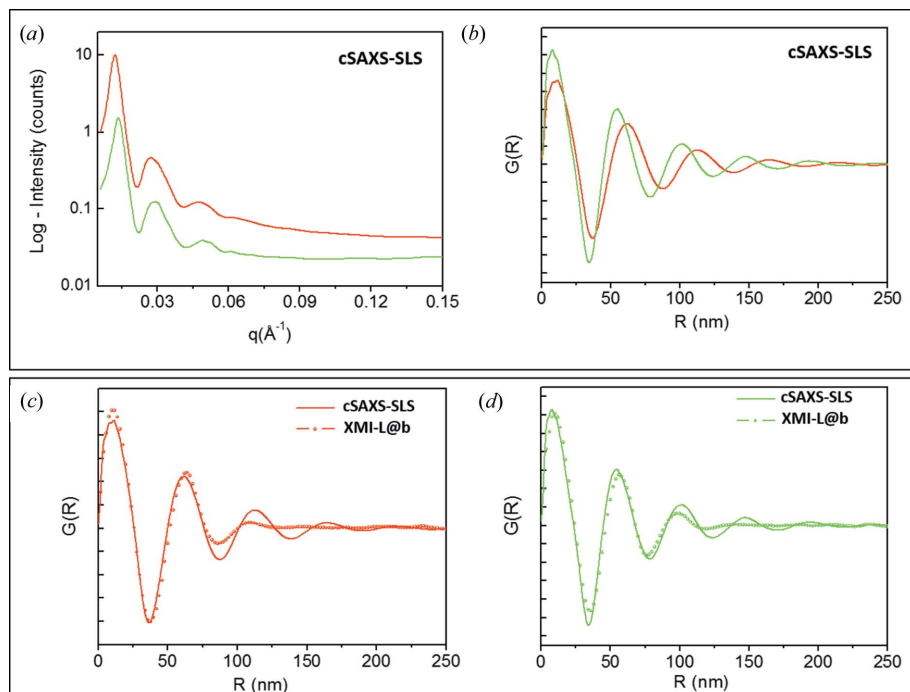


Figure 1

(a) cSAXS-SLS reference data, as selected by adaptive binning from the cSAXS-SLS data set: blue background, red and green SAXS profiles corresponding to the two-dimensional SAXS data of the insets; (b) results of the canonical correlation analysis on the explored area (cSAXS-SLS data set), with the red color corresponding to the red profile in (a) and marking the outer corona without epithelium layer and the green color corresponding to the green profile in (a) in the center of the cornea; (c) cSAXS-SLS (left) and XMI-L@b (right) reference data for the red profile marking the outer corona without epithelium layer; (d) cSAXS-SLS (left) and XMI-L@b (right) reference data for the green profile marking the center of the cornea. Black lines are the filtered cSAXS-SLS and de-noised XMI-L@b reference data.



**Figure 2**  
 (a) Filtered cSAXS-SLS reference data; (b) PDF data extracted from profiles in (a); (c) and (d) comparisons between PDF profiles obtained from the cSAXS-SLS and XMI-L@b data sets.

intensity, *i.e.* the distances between pairs of scattering centers (here fibrils), contained in the scattering volume. The PDF profiles for the cSAXS-SLS filtered data are shown in Fig. 2(b). A similar procedure was also carried out for the XMI-L@b data set. Figs. 2(c) and Fig. 2(d) represent the comparison between the PDF profiles obtained from the cSAXS-SLS and XMI-L@b data sets.

Figs. 3(a) and 3(b) show the PDF profiles, from the cSAXS-SLS and XMI-L@b data sets, with overlaid dotted lines, labelled as  $L$ ,  $\sqrt{3}L$ ,  $2L$ ,  $\sqrt{7}L$ ,  $3L$  *etc.* These lines correspond to the PDF peak positions computed for an ideal array of fibrils packed according to a centered hexagonal symmetry, as pictorially described in Fig. 3(c). In the model  $L$  represents the interfibrillar distance, and each fibril is made up of a core with diameter  $\varphi$  and a shell of thickness  $S$  (see inset of Fig. 3c). The shell value can be extracted from the position of the first PDF peak, whereas the diameter  $\varphi$  can be determined as the

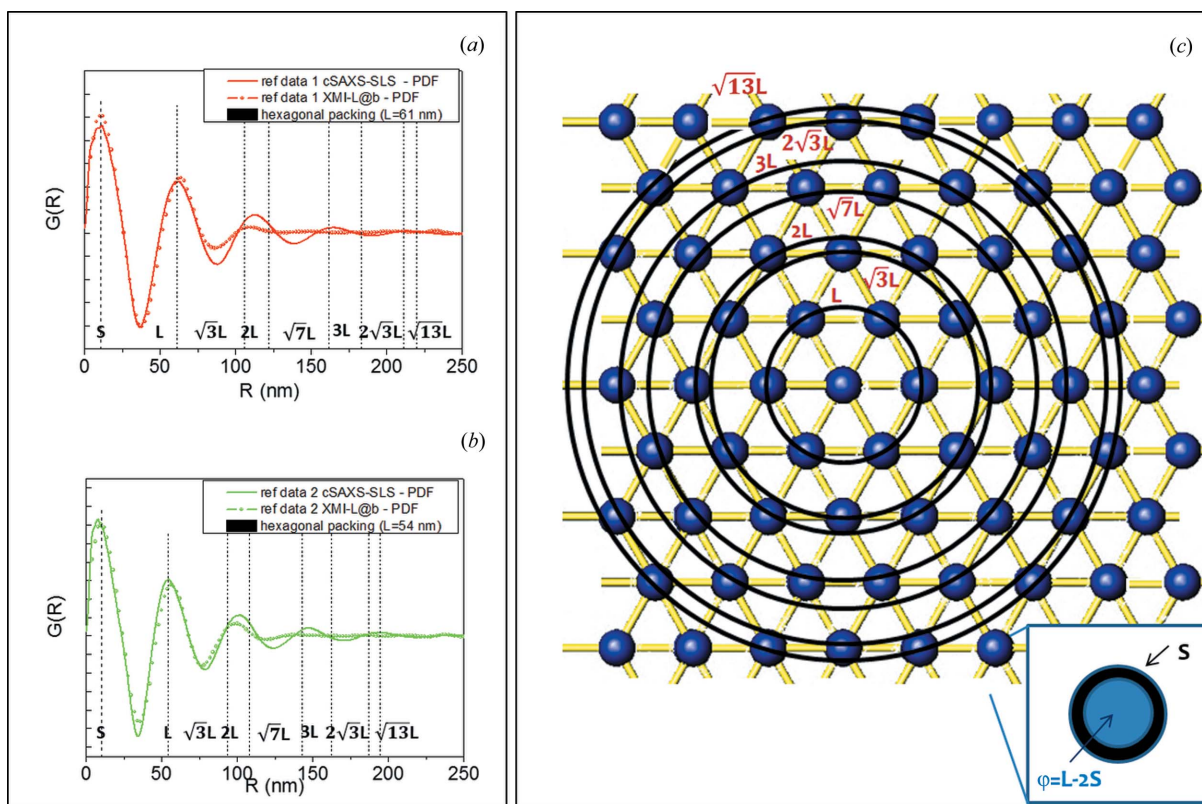


**Figure 3**  
 (a), (b) Comparison between PDF profiles obtained from the cSAXS-SLS and XMI-L@b data sets; (c) pictorial model of the position of an array of fibrils packed according to a centered hexagonal symmetry. The inset shows a typical fibril, which is made up of a core with diameter  $\varphi = L - 2S$  and a shell of thickness  $S$ .

**Table 2**

The shell thickness  $S$ , interfibrillar distance  $L$  and fibril diameter  $\varphi$ , derived from PDF analysis of the cSAXS-SLS and XMI-L@b data sets.

	$S$ (nm)	$L$ (nm)	$\varphi = L - 2S$ (nm)
cSAXS-SLS – outer zone	$11.5 \pm 1$	$62 \pm 1$	$39 \pm 3$
cSAXS-SLS – cross-linked zone	$9 \pm 1$	$56 \pm 1$	$38 \pm 3$
XMI-L@b – outer zone	$11.5 \pm 1.5$	$63 \pm 1.5$	$40 \pm 4.5$
XMI-L@b – cross-linked zone	$10 \pm 1.5$	$57 \pm 1.5$	$36 \pm 4.5$

difference  $\varphi = L - 2S$ . Table 2 summarizes the fibril shell, the interfibrillar distance and the fibril diameter, derived from the PDF analysis of the cSAXS-SLS and XMI-L@b data sets, which characterize the cornea structure in the red corona and green central area of Fig. 1(b). A good correspondence was found between synchrotron and laboratory data.

#### 4. Discussion

Both synchrotron and laboratory data revealed the following:

(a) There is a decrease in the interfibrillar distance and in the shell thickness around the fibrils from the periphery to the center of the cornea; the central area coincides with the region ( $\sim 10$  mm) where the epithelium has been removed for the CXL treatment.

(b) No significant change in the diameter of the fibrils was measured across the explored area.

(c) The array of fibrils resulted in a packing according to a centered hexagonal symmetry (in first approximation, see more below).

The three major findings of our analysis, extracted from both laboratory and synchrotron-radiation data sets, are validated by the literature. Indeed, the decrease of the interfibrillar distance  $L$  from  $\sim 62$  nm (outer corona) to  $\sim 56$  nm (center of the cornea) found from our PDF analysis confirms the same trend reported by Ho *et al.* (2014), Freund *et al.* (2008) and Cheng & Pinsky (2013). In the latter work, the same PDF approach was adopted to evaluate the radial distribution function  $g(r)$  from electron micrographs on human cornea. Secondly, the decrease in the shell thickness of about 15–20% determined by our approach can be ascribed to the effect of cross-linking within proteoglycan core proteins (intraproteoglycan and interproteoglycan cross-links), as reported in the literature (Hayes *et al.*, 2013). Lastly, the core diameter, derived as the difference between the interfibrillar distance and the shell thickness,  $\varphi = L - 2S \sim 36$ –40 nm, was found to be equal in the explored area. Concerning this result, Ho *et al.* (2014) showed that the collagen fibril diameter of bovine cornea stayed constant at a value of around 36–38 nm across the entire area of the tissue.

Finally, in order to explore the validity of the structural model adopted to describe the PDF data, we derived simulated PDF data assuming that the fibrils are assembled according to either a centered hexagonal (Fig. 4a) or a Fibonacci packing (Fig. 4b), the latter being a reliable description of the fibril packing over larger areas (Lewis *et al.*, 2010; Meek & Knupp, 2015). The radially integrated profiles derived from Figs. 4(a) and 4(b) have been compared with the PDF data extracted from the untreated peripheral zone of the cornea, *i.e.* with the red profiles of Fig. 3(a) (cSAXS-SLS data set), and with the PDF data extracted from the cross-linked zone, *i.e.* with the green profiles of Fig. 3(b) (cSAXS-SLS data set). This comparison, displayed in Figs. 4(c) and 4(d), respectively, allows us to conclude that the hexagonal packing better explains the actual order in the cornea, especially in the area treated with riboflavin and UVA.

#### 5. Conclusions

The main aim of the presented work was to propose a procedure, based on statistical (adaptive binning and canonical correlation analysis) and crystallographic (pair distribution function analysis) approaches, to investigate the collagen ultrastructure in cornea. Cornea tissue is a particularly suitable

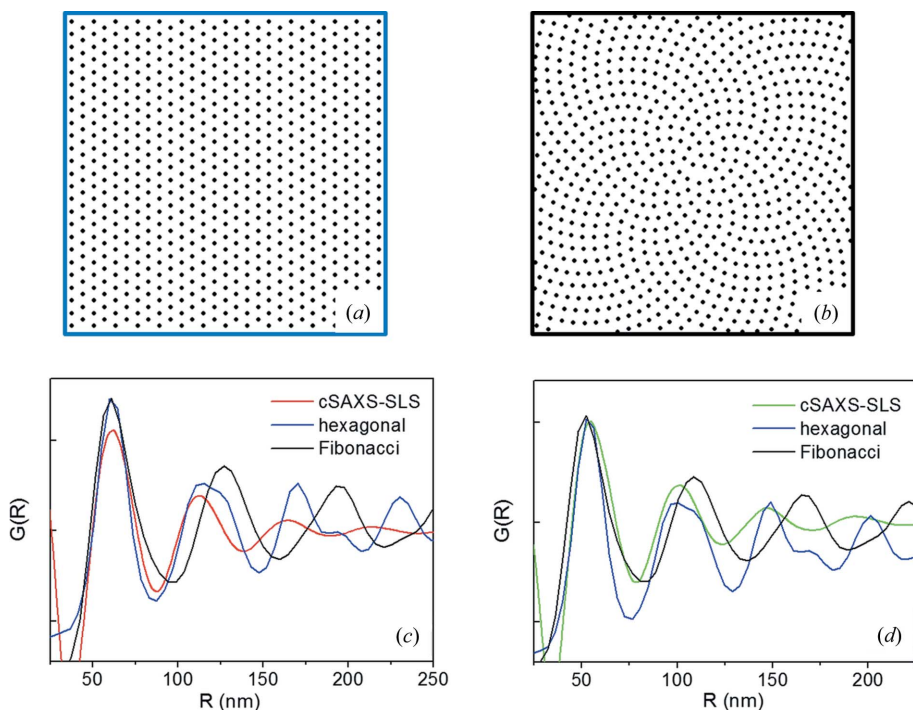


**Figure 4**

(a) Centered hexagonal fibril packing; (b) Fibonacci fibril packing; (c) radially integrated profiles, derived from (a) and (b), here blue and black profiles, respectively, compared with the PDF data extracted from the untreated peripheral zone of the cornea, *i.e.* with the red profiles of Fig. 3(a) (cSAXS-SLS data set); (d) radially integrated profiles, derived from (a) and (b), here blue and black profiles, respectively, compared with the PDF data extracted from the cross-linked zone, *i.e.* with the green profiles of Fig. 3(b) (cSAXS-SLS data set).

model of study thanks to the huge number of results available in the literature. The same cornea was explored by scanning SAXS microscopy with both a table-top and a synchrotron X-ray microsource to obtain a direct comparison between data sets of different quality. Several studies have already demonstrated the suitability of synchrotron-radiation X-ray diffraction methods (Meek & Fullwood, 2001; Meek & Boote, 2009; Meek, 2009; Boote *et al.*, 2003; Meek & Fullwood, 2001; Meek *et al.*, 1991; Meek & Knupp, 2015; Fratzl & Daxer, 1993) to obtain ultrastructure details and quantitative information on the molecular structure of cornea. Therefore, synchrotron data and the literature were used to validate the method proposed here and applied to inspect the lateral packing of the collagen microfibrils in the cornea ultrastructure, and to prove that reliable data can also be extracted with laboratory instrumentation. Considering the technical details reported in Table 1, laboratory instrumentation needs a much longer total acquisition time and shows a clear limitation of maximum length visibility ( $d_{\max} = 2\pi/q_{\min}$ ). However, there are some research projects which cannot be implemented at a synchrotron beamline, because they need a systematic and dedicated daily effort to achieve quantitative and statistical information. For this type of study, table-top instrumentation could still be a valid opportunity.

### Acknowledgements

The authors would like to thank the project ‘Tecnologie Abilitanti per Produzioni Agroalimentari Sicure e Sostenibili’ (TAPASS)-PELM994 (CUP B38C14002040008) funded by Regione Puglia, Area politiche per lo Sviluppo economico, il lavoro e l’innovazione in the framework of the grant ‘Aiuti a Sostegno dei Cluster Tecnologici Regionali per l’Innovazione’, the PRIN 2012 project ‘NOXSS – X-ray Single Shots of Nano Objects’ and the European Commission under the Seventh Framework Programme by means of the grant agreement for the Integrated Infrastructure Initiative No. 262348 European Soft Matter Infrastructure (ESMI). GS acknowledges support from the National Institutes of Health (R21EY023043). Rocco Lassandro, Lucrezia Cassano and Brunella Aresta are acknowledged for technical and administrative support with the XMI-L@b. Keith M. Meek and Carlo Knupp are acknowledged for fruitful discussions.

### References

Altamura, D., Holý, V., Siliqi, D., Lekshmi, I., Nobile, C., Maruccio, G., Cozzoli, P., Fan, L., Gozzo, F. & Giannini, C. (2012). *Cryst. Growth Des.* **12**, 5505–5512.  
 Altamura, D., Lassandro, R., Vittoria, F. A., De Caro, L., Siliqi, D., Ladisa, M. & Giannini, C. (2012). *J. Appl. Cryst.* **45**, 869–873.  
 Aptel, F., Olivier, N., Deniset-Besseau, A., Legeais, J., Plamann, K., Schanne-Klein, M. & Beaurepaire, E. (2010). *Invest. Ophthalmol. Vis. Sci.* **51**, 2459–2465.  
 Birk, D., Fitch, J., Babiarz, J., Doane, K. & Linsenmayer, T. (1990). *J. Cell Sci.* **95**, 649–657.

Blanton, T., Huang, T., Toraya, H., Hubbard, C. R., Robie, S. B., Louër, D., Göbel, H. E., Will, G., Gilles, R. & Raftery, T. (1995). *Powder Diffr.* **10**, 91–95.  
 Boote, C., Dennis, S., Newton, R., Puri, H. & Meek, K. (2003). *Invest. Ophthalmol. Vis. Sci.* **44**, 2941–2948.  
 Boote, C., Dooley, E., Gardner, S., Kamma-Lorger, C., Hayes, S., Nielsen, K., Hjortdal, J., Sorensen, T., Terrill, N. J. & Meek, K. M. (2013). *PLoS One*, **8**, e68166.  
 Boote, C., Kamma-Lorger, C. S., Hayes, S., Harris, J., Burghammer, M., Hiller, J., Terrill, N. J. & Meek, K. M. (2011). *Biophys. J.* **101**, 33–42.  
 Bunk, O., Bech, M., Jensen, T. H., Feidenhans'l, R., Binderup, T., Menzel, A. & Pfeiffer, F. (2009). *New J. Phys.* **11**, 123016.  
 Cheng, X. & Pinsky, P. (2013). *J. R. Soc. Interface*, **10**, 20130512.  
 Daxer, A. & Fratzl, P. (1997). *Invest. Ophthalmol. Vis. Sci.* **38**, 121–129.  
 De Caro, L., Altamura, D., Sibillano, T., Siliqi, D., Filogrosso, G., Bunk, O. & Giannini, C. (2013). *J. Appl. Cryst.* **46**, 672–678.  
 De Caro, L., Altamura, D., Vittoria, F. A., Carbone, G., Qiao, F., Manna, L. & Giannini, C. (2012). *J. Appl. Cryst.* **45**, 1228–1235.  
 Dhaliwal, J. & Kaufman, S. (2009). *Cornea*, **28**, 62–67.  
 Fratzl, P. & Daxer, A. (1993). *Biophys. J.* **64**, 1210–1214.  
 Freund, D., McCally, R., Farrell, R., Cristol, S., L’Hernault, N. & Edelhauser, H. (2008). *Invest. Ophthalmol. Vis. Sci.* **36**, 1508–1523.  
 Fullwood, N. & Meek, K. (1993). *J. Microsc.* **169**, 53–60.  
 Guagliardi, A., Giannini, C., Ladisa, M., Lamura, A., Laudadio, T., Cedola, A., Lagomarsino, S. & Cancedda, R. (2007). *J. Appl. Cryst.* **40**, 865–873.  
 Hayes, S., Boote, C., Kamma-Lorger, C., Rajan, M., Harris, J., Dooley, E., Hawksworth, N., Hiller, J., Terill, N. J., Hafezi, F., Brahma, A. K., Quantock, A. J. & Meek, K. M. (2011). *PLoS One*, **6**, e22405.  
 Hayes, S., Kamma-Lorger, C., Boote, C., Young, R., Quantock, A., Rost, A., Khatib, Y., Harris, J., Yagi, N., Terrill, N. & Meek, K. (2013). *PLoS One*, **8**, e52860.  
 Ho, L., Harris, A., Tanioka, H., Yagi, N., Kinoshita, S., Caterson, B., Quantock, A. J., Young, R. D. & Meek, K. M. (2014). *Matrix Biol.* **38**, 59–68.  
 Hotelling, H. (1936). *Psychometrika*, **1**, 27–35.  
 Huang, Y., Tuft, S. & Meek, K. (1996). *Cornea*, **15**, 320–328.  
 Juhás, P., Davis, T., Farrow, C. L. & Billinge, S. J. L. (2013). *J. Appl. Cryst.* **46**, 560–566.  
 Komai, Y. & Ushiki, T. (1991). *Invest. Ophthalmol. Vis. Sci.* **32**, 2244–2258.  
 Lewis, P., Pinali, C., Young, R. D., Meek, K. M., Quantock, A. J. & Knupp, C. (2010). *Structure*, **18**, 239–245.  
 Marshall, G., Konstas, A. & Lee, W. (1991a). *Graefes Arch. Clin. Exp. Ophthalmol.* **229**, 157–163.  
 Marshall, G., Konstas, A. & Lee, W. (1991b). *Graefes Arch. Clin. Exp. Ophthalmol.* **229**, 164–171.  
 Masters, B. (2009). *J. Biophotonics*, **2**, 127–139.  
 Maurice, D. (1957). *J. Physiol.* **136**, 263–286.  
 Maurice, D. (1962). *Int. Ophthalmol. Clin.* **2**, 561–572.  
 Maurice, D. (1984). *The Eye*, edited by H. Davson. New York, London: Academic Press.  
 Maurice, D., Zhao, J. & Nagasaki, T. (2004). *Exp. Eye Res.* **78**, 591–597.  
 Meek, K. (2009). *Biophys. Rev.* **1**, 83–93.  
 Meek, K. & Boote, C. (2009). *Prog. Retin. Eye Res.* **28**, 369–392.  
 Meek, K. & Fullwood, N. (2001). *Micron*, **32**, 261–272.  
 Meek, K., Fullwood, N., Cooke, P., Elliott, G., Maurice, D., Quantock, A., Wall, R. & Worthington, C. (1991). *Biophys. J.* **60**, 467–474.  
 Meek, K., Hayes, S., Kamma-Lorger, C., Boote, C. & Quantock, A. (2008). *Invest. Ophthalmol. Vis. Sci.* **49**, 3913.  
 Meek, K. & Knupp, C. (2015). *Prog. Retin. Eye Res.* **49**, 1–16.  
 Meek, K. & Quantock, A. (2001). *Prog. Retin. Eye Res.* **20**, 95–137.



- Meek, K., Quantock, A., Elliott, G., Ridgway, A. E. A., Tullo, A., Bron, A. & Thonar, E. (1989). *Exp. Eye Res.* **49**, 941–958.
- Meek, K., Tuft, S., Huang, Y., Gill, P., Hayes, S., Newton, R. & Bron, A. (2005). *Invest. Ophthalmol. Vis. Sci.* **46**, 1948–1956.
- Quantock, A., Fullwood, N., Thonar, E., Waltman, S., Capel, M., Ito, M., Verity, S. & Schanzlin, D. (1997). *Eye*, **11**, 57–67.
- Quantock, A., Meek, K., Brittain, P., Ridgway, A. E. A. & Thonar, E. (1991). *Tissue Cell*, **23**, 593–606.
- Quantock, A., Meek, K., Fullwood, N. & Zabel, R. (1993). *Can. J. Ophthalmol.* **28**, 266–272.
- Quantock, A., Meek, K., Ridgway, A. E. A., Bron, A. & Thonar, E. (1990). *Curr. Eye Res.* **9**, 393–398.
- Quantock, A., Meek, K., Thonar, E. & Assil, K. (1993). *Eye*, **7**, 779–784.
- Rawe, I., Leonard, D., Meek, K. & Zabel, R. (1997). *Cornea*, **15**, 369–376.
- Scarcelli, G., Besner, S., Pineda, R., Kalout, P. & Bron, A. (2015). *JAMA Ophthalmol.* **133**, 480–482.
- Scarcelli, G., Besner, S., Pineda, R. & Yun, S. H. (2014). *Invest. Ophthalmol. Vis. Sci.* **55**, 4490–4495.
- Scarcelli, G., Pineda, R. & Yun, S. (2012). *Invest. Ophthalmol. Vis. Sci.* **53**, 185–190.
- Sibillano, T., De Caro, L., Altamura, D., Siliqi, D., Ramella, M., Boccafoschi, F., Ciasca, G., Campi, G., Tirinato, L., Di Fabrizio, E. & Giannini, C. (2014). *Sci. Rep.* **4**, 6985.
- Siliqi, D., De Caro, L., Ladisa, M., Scattarella, F., Mazzone, A., Altamura, D., Sibillano, T. & Giannini, C. (2016). *J. Appl. Cryst.* **49**, 1107–1114.
- Snibson, G. (2010). *Clin. Exp. Ophthalmol.* **38**, 141–153.
- Spoerl, E., Huhle, M. & Seiler, T. (1998). *Exp. Eye Res.* **66**, 97–103.
- Spoerl, E., Wollensak, G. & Seiler, T. (2004). *Curr. Eye Res.* **29**, 35–40.
- Wollensak, G. (2006). *Curr. Opin. Ophthalmol.* **17**, 356–360.
- Wollensak, G., Spoerl, E. & Seiler, T. (2003a). *Am. J. Ophthalmol.* **135**, 620–627.
- Wollensak, G., Spoerl, E. & Seiler, T. (2003b). *J. Cataract Refract. Surg.* **29**, 1780–1785.
- Zhan, O., Burrows, R. & Cintron, C. (1990). *Exp. Eye Res.* **60**, 551–561.
- Zimmermann, D., Trüeb, B., Winterhalter, K., Witmer, R. & Fischer, R. (1986). *FEBS Lett.* **197**, 55–58.